JOURNAL OF PROPULSION AND POWER
Vol. 26, No. 6, November–December 2010

Inlet Starting of High-Contraction Axisymmetric Scramjets

Hideaki Ogawa,* Alexander L. Grainger,† and Russell R. Boyce‡
University of Queensland, Brisbane, Queensland 4072, Australia

DOI: 10.2514/1.48284

Reliable in-flight starting of the inlet is of critical importance for the successful operation of scramjet engines, particularly axisymmetric configurations with high-contraction inlets. The present research is undertaken to examine the capability of various inlet starting methods based on two principles: unsteady flow effects and variable geometries. Time-accurate viscous computations have been performed to investigate the transitional flowfields introduced by a variety of methods that are applicable to axisymmetric geometries. Parametric studies have been conducted for instantaneous rupture of conical diaphragms and addition of bleed slots, which induce highly unsteady flow phenomena. Several methods employing variable inlet geometries have been tested for the latter principle, including opening doors and sliding doors (or diaphragm erosion). Successful inlet starting has been achieved as a result of unsteady transition induced by diaphragm rupture and quasi-steady transition, due to the sliding-door opening process. In particular, a bleed addition to the diaphragm rupture method has been found to be highly effective and pronounced flow stability has been observed in the sliding-door process.

Nomenclature

A_i	=	cross-sectional area at the inlet entrance, m^2
A^*	=	cross-sectional area at the inlet exit, m^2
m_{in}	=	mass flow rate of the inflow (at the inlet entrance), kg/s
m_{out}	=	mass flow rate of the outflow (at the inlet exit), kg/s
M_∞	=	freestream Mach number
p	=	static pressure, Pa
p_c	=	static pressure at conical diaphragm surface (upstream), Pa
p_i	=	internal stagnation pressure, Pa
p_{0c}	=	total static pressure at conical diaphragm surface (upstream), Pa
$p_{0\infty}$	=	freestream total static pressure, Pa
p_∞	=	freestream static pressure, Pa
r	=	radial coordinate, m
T_∞	=	freestream static temperature, K
t	=	time in transient flowfields, ms
x	=	streamwise coordinate, m
θ	=	conical diaphragm angle, °
θ_s	=	shock wave angle, °

I. Introduction

HYPERSONIC airbreathing propulsion offers great potential for reliable and economical access to space as well as atmospheric flight. In particular, scramjets (supersonic combustion ramjets) are a promising technology that can enable efficient and flexible transport systems by removing the need to carry oxidizers and other propulsion limitations of conventional rocket engines. Supersonic combustion via the use of scramjet technology was successfully demonstrated for the first time worldwide by the HyShot II Program in July 2002 [1,2], followed by successful flights of the Hyper-X vehicles at Mach 6.8 (March 2004) and Mach 9.6 (November 2004) [3].

A simple axisymmetric scramjet configuration (Fig. 1) is currently being explored, with promising performance demonstrated in shock tunnel testing [4]. Figure 2 illustrates a schematic diagram of an axisymmetric scramjet engine, which operates in a sequential process: hypersonic inflow is compressed to a desired higher pressure (and consequently high temperature) at the exit of the inlet, which induces combustion in the downstream chamber. The reacted gas expands in the nozzle to produce thrust. Combined with several innovative concepts such as upstream fuel injection in the inlet and radical-farming shock-induced combustion, this elegantly simple geometry can bring numerous advantages over three-dimensional geometries in aerodynamic and combustion efficiency, aerothermal and structural management, and manufacture [5,6].

In spite of these merits, however, high-internal-compression axisymmetric inlets are inherently difficult to start spontaneously during flight. The flow inside the scramjet engine must be supersonic throughout in normal operation in the started case. However, high-contraction inlets can also operate in an unstarted mode, where the flow choke at the exit of the inlet leads to a subsonic inlet and a strong bow shock formed upstream of the inlet, resulting in dramatic reduction in inlet mass capture and thus engine thrust. This *inlet starting* issue is intrinsic to internal-compression axisymmetric geometries, because the structure does not allow surplus mass flow to spill overboard [7]. The possibilities of these flow regimes are prescribed by the isentropic and Kantrowitz theory with respect to the inflow Mach number M_∞ and area contraction ratio A_i/A^*, based on quasi-steady inviscid one-dimensional-flow assumptions [8,9]. Figure 3 shows three domains divided by two curves; the inlet always starts spontaneously above the Kantrowitz line, because mild contraction allows larger mass flow than the choking limit. Below the isentrope line, on the other hand, high compression due to a small area ratio always prohibits the inlet from starting, due to too little mass flow entry. Both started and unstarted states are possible in the region bounded by the two curves, which is the zone of interest, because the majority of practical scramjets fall into this area. Unstarted flow is predominantly experienced by high-compression inlets in in-flight operation, thus requiring auxiliary methods to start the inlet, where supersonic started flow can be sustained once it is established.

A variety of methods for starting high-compression inlets have been developed, due to the importance of this issue. Classical and conventional methods have been contrived to overcome the Kantrowitz limit within quasi-steady assumptions. Examples include overspeeding and mass flow spillage. The former technique attains started flow by temporarily accelerating the vehicle to surpass the Kantrowitz limit [9], but this is only relevant for low supersonic Mach numbers and mild inlet conditions. The latter aims to achieve

Presented as Paper 2009-7401 at the 16th AIAA/DLR/DGLR International Space Planes and Hypersonic Systems and Technologies Conference, Bremen, Germany, 19–22 October 2009; received 19 January 2010; revision received 13 April 2010; accepted for publication 20 April 2010.

*Postdoctoral Research Fellow, Centre for Hypersonics, School of Mechanical and Mining Engineering. Member AIAA.

†Postgraduate Research Student, Centre for Hypersonics, School of Mechanical and Mining Engineering.

‡Professor, DSTO Chair for Hypersonics, Centre for Hypersonics, School of Mechanical and Mining Engineering. Senior Member AIAA.

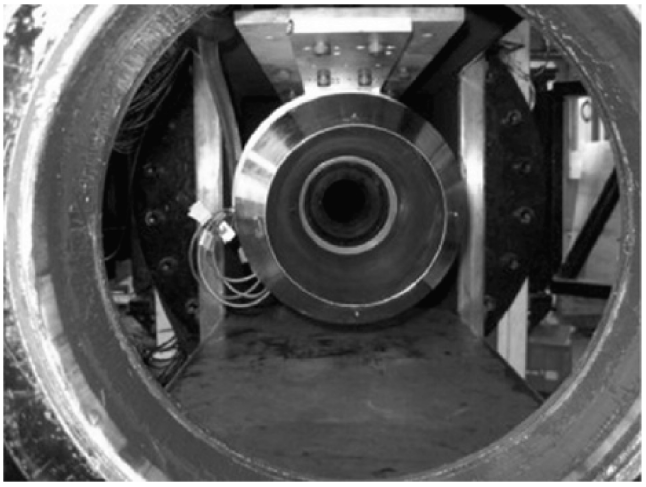

Fig. 1 Axisymmetric scramjet (upstream view).

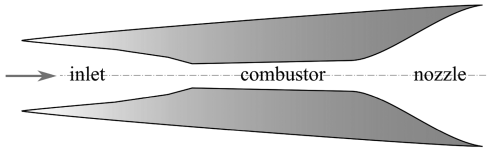

Fig. 2 Schematic diagram of an axisymmetric scramjet.

started flow by adjusting the mass flow rate by using geometric modifications [11,12]. Examples of this category include the modular Busemann inlet, which can induce self-starting while offering the advantage of high performance and design flexibility [13,14]. However, such methods tend to incur major disadvantages, including prohibitive aerothermal heat load and substantial spillage drag under offdesign conditions as well as complexity in manufacture. The implementation of these techniques in scramjet inlets thus represents considerable difficulties from practical standpoints. More viable methods can be categorized into two major classes: *unsteady effects* and *variable geometries*. The former approach makes use of highly unsteady effects to circumvent the quasi-steady assumptions, and hence the Kantrowitz limit, by employing such methods as instantaneous rupture of temporary diaphragms sealing the inlet, and enormous acceleration of the vehicle [7,15,16]. In the latter approach, the mass flow entry is regulated by altering the effective area for the inflow by means of additional devices installed in the inlet such as opening doors and tractor rocket plugs [17]. However, the capability of these methods to start the inlet has only been demonstrated in inviscid numerical simulations, and no computational effort has so far been dedicated to investigate their effectiveness in the presence of viscous effects.

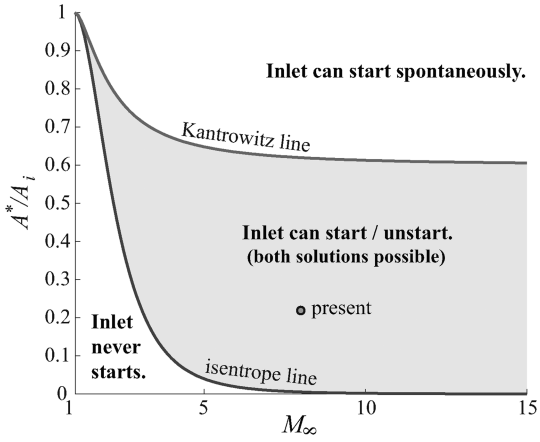

Fig. 3 Possible flow regimes in supersonic/hypersonic inlets (after [10]).

The present research has been undertaken to examine the axisymmetric inlet starting capability of various methods by means of unsteady flow effects and variable geometries and to identify the underlying physics as well as key factors in the inlet starting process, including viscous effects, which were found to exert a crucial impact on the inlet startability in a preceding study conducted by the authors [18]. This paper presents the results of time-accurate computational simulations of the transient flowfields introduced by several selected methods that are particularly suitable and feasible for implementation to axisymmetric scramjets: i.e., diaphragm rupture (with/without mass bleeding), opening doors, and sliding doors.

II. Approaches

A. Configurations

1. Inlet Geometry

The inlet section of an axisymmetric scramjet engine is focused on in this study, its schematic diagram shown in Fig. 4 along with the dimensions assumed here. The inlet has a contraction of 4.8, comprising three ramps and a leading-edge tip radius of 0.5 mm. The conical semivertex angle of the diaphragm (or that of the doors in the case of variable geometries) θ is nominally set to be 35°, which has been found to be the optimum in inviscid parametric studies previously undertaken for a relevant Busemann-type geometry [15], allowing a maximum possible internal pressure behind the diaphragm (p_i) that can be tolerated while still starting the inlet. A small degree of divergence is applied to the combustor section to impose a throat condition at the end of the inlet and thus ensure a supersonic flow regime downstream at the event of inlet starting. An option for a single annular bleed for the boundary layer is included, starting at the junction between the first and second ramps. The size of the bleed is varied between 9.3 and 37% of the length of the second ramp, depending on the case being studied.

2. Flow Conditions

The freestream conditions are $M_\infty = 8.0$, $p_\infty = 1197$ Pa, and $T_\infty = 226.5$ K at an altitude of 30 km above sea level, assuming typical scramjet operation on a constant-dynamic-pressure trajectory of 53.6 kPa. This results in the inlet being located in the dual solution zone, between the isentrope and the Kantrowitz criterion, as per Fig. 3. The Reynolds number based on the inlet exit radius (0.035 m) is $Re_\infty = 1.06 \times 10^5$, assuming standard air for the inflow.

B. Inlet Starting Techniques

1. Diaphragm Rupture

Temporary diaphragm rupture has been found to be one of the promising methods for inlet starting in previous numerical investigations [11]. The essence of this method is to use flow unsteadiness introduced by instantly removing a frangible structure, across which high-pressure gradients are imposed before rupture, as outlined in [11]. A diaphragm is placed at the entrance of the inlet with downstream air stagnant at a given pressure. The diaphragm is then removed instantaneously, resulting in abrupt flow acceleration and formation of the external conical shock layer into the inlet (Fig. 4).

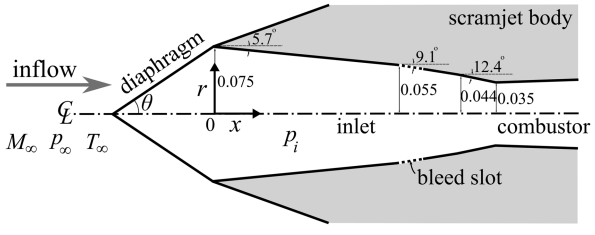

Fig. 4 Inlet geometry and specification (with a conical diaphragm).

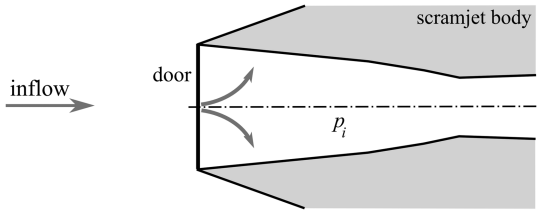

Fig. 5 Opening doors.

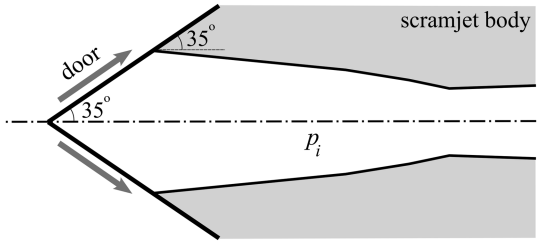

Fig. 6 Sliding doors (diaphragm erosion).

In addition to the nominal semivertex angle θ of 35°, three additional diaphragm angles [i.e., 50, 70, and 90° (normal diaphragm)] have been tested in order to investigate the influence of different flow configurations, where the shock wave can be either attached or detached (and hence weaker or stronger, respectively), depending on the semivertex angle. At Mach 8, the conical shock relations indicate that the before-rupture external shock will be attached for 3 and 50° and will be detached with a subsonic shock layer for 70 and 90°.[§] Various internal diaphragm pressures p_i are examined to find the maximum allowable pressure below which inlet starting occurs.

2. Variable Geometries

Another approach examined in the present study is to attempt to satisfy the Kantrowitz criterion by directly modifying the inlet geometry with a slowly opening inlet to regulate mass flow entry. The methods tested here include opening normal doors and sliding doors (or erosion of the conical diaphragm from its tip).[¶] Relatively slow movement of the inlet components is employed to cause the flowfields to transition in a quasi-steady manner rather than unsteady. The configurations of these methods are based on that of diaphragm rupture. The employed methodologies are individually described below.

a. Opening Doors. The inlet is initially sealed with a thin door (1 mm in thickness), one end of which is hinged at the top of the inlet entrance. Figure 5 illustrates the principle of this method. The door is released to allow mass flow to enter, rotating about the hinge at a constant angular acceleration so that the door fully opens in 50 ms. The internal pressure p_i downstream of the door is set to 65% of the freestream.

b. Sliding Doors. The inlet is initially covered by a flat door with the same dimensions as the diaphragm used in the previous section, apart from a definite thickness of 1 mm. The door slides upward at a constant velocity (Fig. 6), increasing the aperture for mass flow entry, so that a fully open inlet is achieved in 50 ms. The internal pressure p_i downstream of the door is 65% of the freestream value. The slope of the external contour of the inlet is modified to 35° in this particular case in order to accommodate the retrieving door without extrusion. This method is analogous to the erosion of a temporary conical diaphragm that gradually melts off from the tip, due to the aerodynamic heat load undergone at the stagnation point.

[§]The maximum conical diaphragm angle for attached shock waves is 56° at $M_\infty = 8$, as shown in Sec. III.A.1, according to the conical shock relations.

[¶]Practical implementation of these methods is not considered in the present study, which is primarily aimed at preliminary investigation of the capability of each concept.

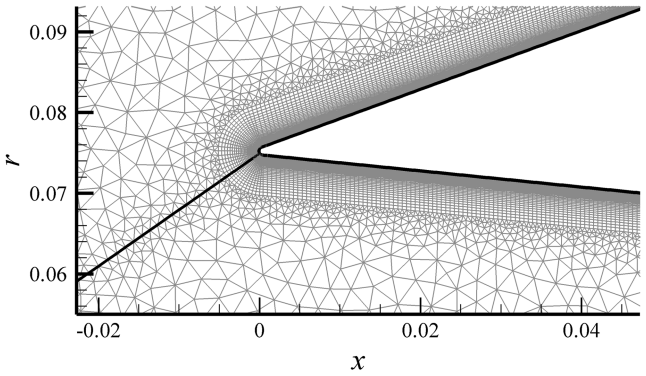

Fig. 7 Hybrid mesh (near the leading edge).

C. Numerical Modeling

1. Computational Method

The compressible Navier–Stokes equations are solved for steady and transient flowfields by using a commercial code CFD++ [19]. Subjected to rigorous code validation studies, this solver has been employed with great success on relevant hypersonic problems in the past [2,20]. An implicit algorithm with second-order spatial accuracy is used for steady computation and transient flowfields are computed in a time-accurate manner using the first-order global time marching with a time step of 0.01 ms over a maximum time period of 6 ms for the diaphragm method and a time step of 0.1 ms over time periods of 80–150 ms for variable-geometry methods. Multigrid convergence acceleration is employed and the transient flowfield is converged at every global time step by inner iterations of up to 50 steps. Centroidal extrapolation is used for the exit boundary of the internal flow, and supersonic outflow is assumed for the outlet of the external flow domain. The body surface of the scramjet as well as that of the solid structures (e.g., diaphragm, doors) are assumed to be adiabatic.

The fluid is treated as a compressible perfect gas with compositions of standard air. The two-equation cubic k-ε Reynolds-averaged Navier–Stokes model is adopted for turbulence modeling, where nonlinear terms account for normal-stress anisotropy, swirl, and streamline curvature effects. An advanced two-layer wall function in the equilibrium/nonequilibrium blend mode is employed to ensure prediction accuracy of wall fluxes for momentum and energy in the viscous sublayer and buffer layer on fine grids ($0.1 \leq y^+ \leq 50$) as well as the logarithmic overlap region on coarse ones ($50 \leq y^+ \leq 300$). Fully turbulent flow is assumed for the freestream, with the turbulence kinetic energy k_∞ and dissipation rate ε_∞ set to 3.45×10^3 m^2/s^2 and 1.35×10^8 m^2/s^3, respectively, and no transition specifically imposed on the boundary layer.[**]

The instantaneous removal of the diaphragm is simulated by replacing the wall boundary condition with a simple flow-through zonal boundary in the transient computation. Boundary-layer bleeding is simulated by imposing a supersonic outflow boundary condition on the slot. The motion of movable components, i.e., doors, is achieved by means of the moving-mesh capability of CFD++, where the secondary mesh moves at the desired translational or rotational velocities and flow properties in the overlapping regions with the background mesh are interpolated via use of overset zonal boundary conditions.

2. Computational Mesh

Computational grids are generated with the aid of a commercial meshing tool Pointwise [21]. Hybrid grids are used in this study, as shown in Fig. 7, which shows the mesh structure in the leading-edge region. Quadrilateral structured cells are used in the vicinity of the walls to better capture the characteristics of the boundary-layer flows, particularly with respect to separation, whereas the regions away from the walls are represented by triangle unstructured cells. The

[**]The state of the boundary layer, i.e., laminar/turbulent, has been found to exert rather minor impact on the transient flowfields in the preceding study [18].

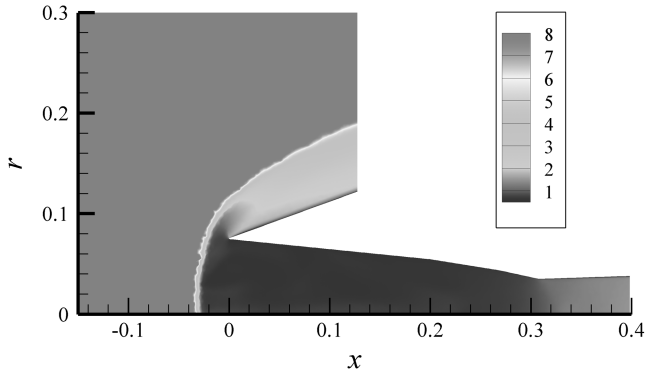

a) Coarse mesh

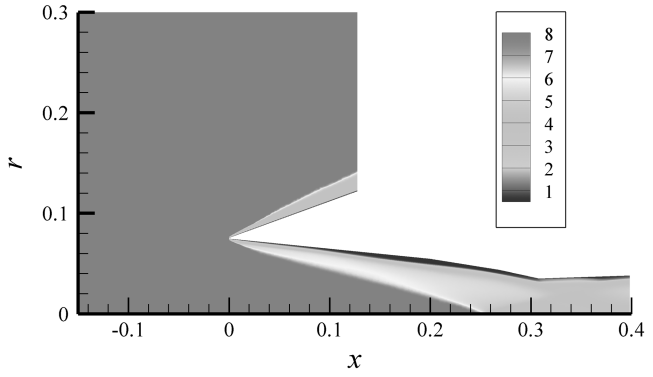

b) Fine mesh

Fig. 8 Flowfields at $t = 6$ ms after diaphragm rupture with different mesh resolutions (Mach number distributions).

only exception is the near-surface region of the diaphragm, along which unstructured grids are employed in order to avoid meshing complexity, on the assumption that the global mechanism of the inlet starting process be little affected by the state of the boundary layer on the diaphragm. The boundary-layer regions in the vicinity of the surface of the movable components (doors) are represented by structured grids with somewhat reduced resolutions, as compared with the walls of the scramjet body. One end of the diaphragms and moving components is anchored at the center of the leading edge in order to avoid skewness in the structured domain and facilitate meshing.

The mesh resolution has been determined, based on a preliminary mesh sensitivity study. Flowfields are examined for diaphragm rupture at an internal pressure p_i set to 50% of the freestream value p_∞ for three different mesh resolutions: coarse (1892 structured and 20,299 unstructured cells), medium (34,034 structured and 40,396 unstructured cells) and fine mesh (49,441 structured and 72,262 unstructured cells). The axial spacing of the structured mesh on the first ramp is 4.1 mm for the coarse mesh and 0.54 mm for the medium and fine ones. The nondimensional distance y^+ value is 0.32 on average at the first grid point off the wall for all resolutions, ensuring

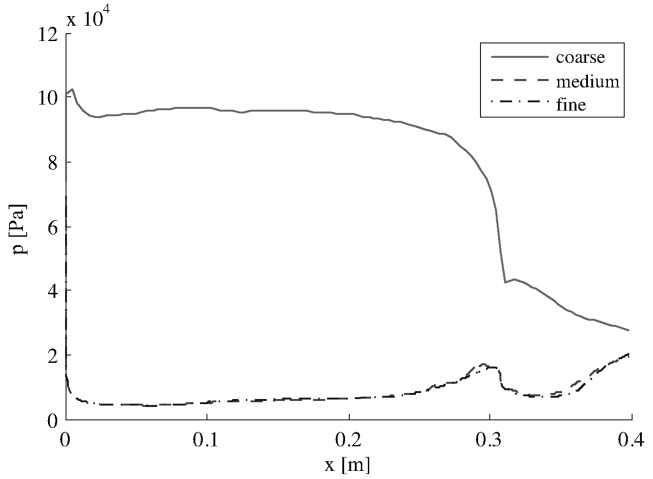

Fig. 9 Comparison of internal surface pressure distributions at $t = 6$ ms between different mesh resolutions.

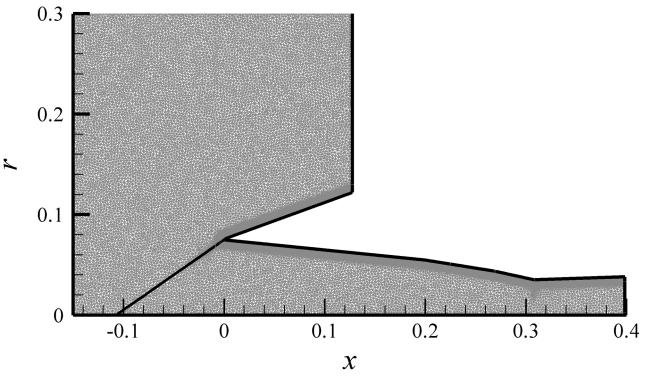

a) Diaphragm rupture (overall)

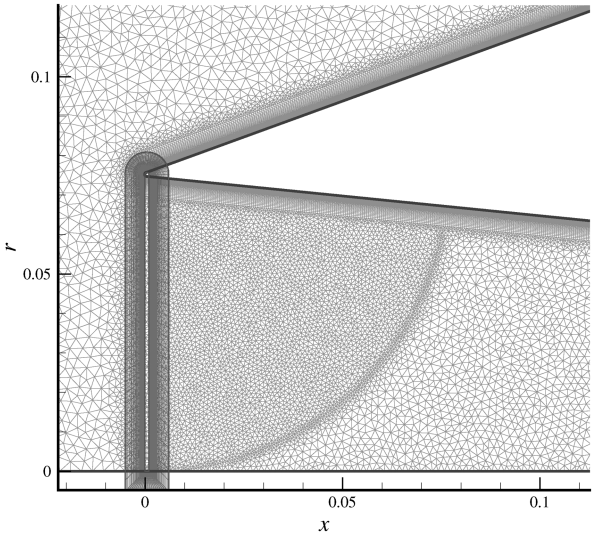

b) Opening doors (close-up)

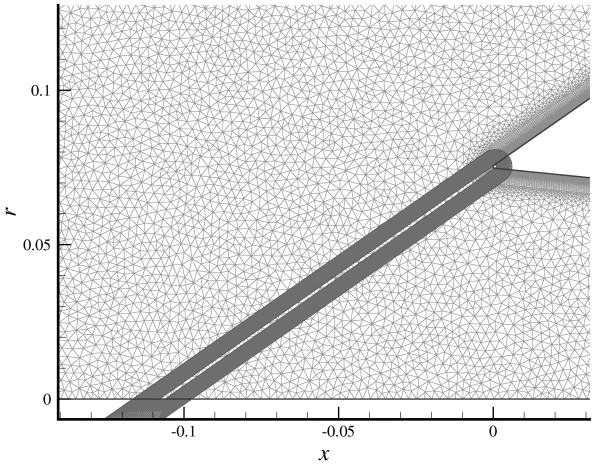

c) Sliding doors (close-up)

Fig. 10 Computational mesh.

good resolution of the viscous sublayer. No discernible difference has been found in the surface pressure distributions in the steady flowfields with the diaphragm on (results are not shown here). However, a remarkable difference has been observed in the transient flowfields; instantaneous diaphragm removal has led to a fully choked flow in the flowfield with a coarse mesh, whereas a steady started inlet has been achieved in the medium- and fine-mesh cases, as shown in Fig. 8.

The surface pressure distributions on the internal walls of the inlet are compared in Fig. 9. Nearly identical distributions can be seen for the medium and fine meshes, while the low resolution of the coarse mesh has resulted in substantially higher pressure, due to the flow choke. The medium mesh, which can strike the balance between the simulation fidelity and computational cost, is thus selected as the standard mesh for the present study. The overall computational domain with this resolution is displayed for the diaphragm rupture method in Fig. 10a.

Figure 10b is a close-up of the computational grids used for the door opening method. A structured mesh comprising 97×30 cells with a minimum cell width of 1×10^{-4} m on the wall is used to resolve the flowfield surrounding the door, whereas the global flowfield is represented by a hybrid mesh, which is based on the mesh used for diaphragm rupture but significantly refined in the domain that the door passes through. This facilitates the interpolation associated with an overset zonal boundary condition, which is applied for the region where the two meshes overlap. Shown in Fig. 10c is a close-up view of the grids used for sliding-door simulation. The surrounding of the door is represented by a structured mesh comprising 437×50 cells with a minimum cell width of 5×10^{-5} m at the wall, linked to the background mesh by an overset zonal boundary condition.

3. *Procedure*

The computational procedure employed in the present study consists of two steps:

1) A steady computation is first performed to establish a steady flowfield in the presence of a solid structure that initially covers the inlet (i.e., diaphragm, doors), behind which air is sealed with the internal pressure p_i set at the desired level. A typical steady solution, for instance, is shown in Fig. 11, which displays the Mach number distribution in the presence of a conical diaphragm with a semivertex angle θ of 70°, leading to a detached bow shock structure, as expected.

2) A time-accurate computation is then performed for the transient flowfield by using the steady solution from the first stage as the initial flowfield. At this stage, the diaphragm is removed by replacing the viscous wall boundary condition with a patched zonal boundary condition to simulate instant diaphragm rupture. Boundary-layer bleeding is achieved by switching the boundary condition of the slot from a viscous wall to a supersonic outflow boundary condition with a fixed back pressure, which is set to the ambient static pressure ($p_\infty = 1197$ Pa). The motion of the variable-geometry components (namely, doors) is activated by turning on the moving-mesh capability.

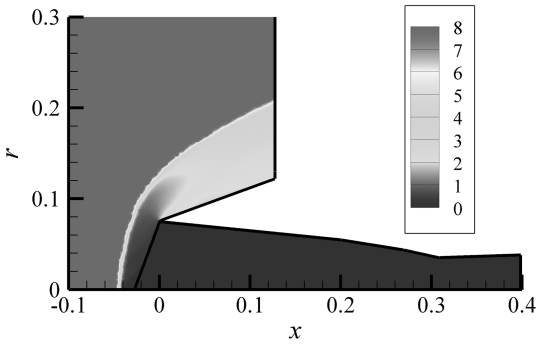

Fig. 11 Steady solution in the presence of conical diaphragm ($\theta = 70°$, Mach number).

III. Results

A. Diaphragm Rupture

1. *Semivertex-Angle Investigation*

a. $\theta = 35°$. The flowfield introduced by the rupture of a conical diaphragm with a semivertex angle θ of 35° has first been examined as a reference case, based on a previous report [15], as described in Sec. II.A.1. It has been found in the preceding study conducted by the authors [18] that the rupture of a conical diaphragm with this angle and an internal pressure of 65% of the freestream value results in an unstarted inlet in the presence of viscous effects. When the internal pressure is decreased to 60%, however, a started solution has been achieved in the present study. This suggests that the maximum internal pressure p_i allowable for this angle to start the inlet lies between 60 and 65% of the freestream value.

Shown in Fig. 12 is the progression of the Mach number distributions for the transitional flowfields introduced by instant removal of a conical diaphragm with internal pressures of 65 and 60% of freestream. It can be seen that the spatial pressure gradients placed across the diaphragm were successful in inducing an initial flow acceleration into the inlet upon rupture in both cases. As is the case for both solutions, an incipient period of flow acceleration caused by the spatial pressure gradients occurs from rupture to approximately $t = 0.7$ ms, with an oblique shock forming at the leading edge, reflecting back off the symmetry axis and toward the scramjet surface and interacting with the boundary layer.

For the unstarted case (Fig. 12a), a large boundary-layer separation region then forms, reaching its zenith at approximately $t = 2$ ms, starting at the first compression corner of the inlet geometry. This region grows and begins to move upstream, with a large recirculation region forming. It can also be observed that as this occurs, the effective contraction ratio of the scramjet inlet is increased, resulting in less mass flow entering the combustion chamber. The relative strength of the oblique shock from the leading edge increases as the boundary layer begins to move upstream, due to the shock profile approaching normality. Consequently, a normal shock forms at the symmetry axis at approximately $t = 3$ ms, which moves upstream and eventually merges with the oblique shock to form a single bow shock. At the same time as the normal shock formation, another normal shock close to the inlet exit has also formed. However, this secondary normal shock becomes obsolete and disappears as the strength of the first shock increases as it moves upstream. The primary normal shock then concatenates with the oblique shock, with this combined shock ultimately positioned in front of the inlet leading edge at 6 ms, resulting in an unstarted solution with subsonic flow entering and dominating the throat. For the started case (Fig. 12b), on the other hand, the upstream motion of the flow after the initial acceleration is suppressed, with a much smaller separation region being formed. As such, the flow reverses once more and continues downstream, with a started solution being attained at $t = 6$ ms after a prior stabilization period. In this case, normal shocks that have been observed at the symmetry axis in the unstarted case are not present, due to the suppression of upstream movement.

To further investigate the flowfields the mass flow rates have been calculated at the streamwise stations of interest. Plotted in Fig. 13 are the mass flow rates of the inflow measured at the inlet entrance ($x = 0$ m) and those of the outflow at the inlet exit ($x = 0.308$ m) for the unstarted ($p_i = 65\%$) and started ($p_i = 60\%$) cases over 6 ms of the computation period. Figure 13a shows the influence of the unstarted flow regime on the mass flow. Following a large peak in the outflow mass rate at approximately $t = 0.7$ ms caused by the initial acceleration that flushes the near-stagnant air into the throat, it is seen that the outflow rate begins to diminish as the separation begins to grow at approximately $t = 2$ ms. As the shock structure approaches the leading edge, the mass flow into the inlet becomes more subject to the choking flowfield, with radical fluctuations being seen after $t = 4.2$ ms and continuing until the end of the computation. In the case of the internal pressure of 60% (Fig. 13b), on the other hand, comparatively high levels of mass flow rates are maintained until the end of the computation time, when both rates match at approximately 0.8 kg/s, the flowfield settling in a steady state. This is indicative of a

steady flow stream that goes through the inlet at a constant mass flow rate and hence of the establishment of a started flow regime. This result implies the starting process has a high sensitivity to the magnitude of the spatial gradients for a conical diaphragm and hence a high dependence upon the initial acceleration of the flow.

b. $\theta = 50°$. In consideration of the trend that the maximum allowable pressure reduces with the conical angle [15], an internal pressure of 50% of the freestream value p_∞ has first been tested for rupture of a diaphragm with a semivertex angle θ of 50°. Initially after rupture, the inflow accelerates into the stagnant section, flushing this region downstream into the combustor section ($t = 0.1$–0.7 ms) with an oblique shock associated with the leading edge reflecting off the symmetry axis downstream. At approximately $t = 2$ ms, a large separated region forms at the first compression corner with the consequence being a higher contraction imposed on the flow, which restricts mass flow into the combustion chamber (Fig. 14a). This separated region continues to grow and moves directly upstream, with a normal shock wave forming near the centreline of the domain ($t = 3.5$ ms, Fig. 14b). This normal shock continues to grow as it moves upstream, changing the profile of the previous oblique shock. The two shock waves merge at approximately $t = 5$ ms, with the flow settling to an unstarted state ($t = 5$–6 ms). The static pressure distributions are plotted in Fig. 15 for the inflow ($x = 0$ m) and outflow at the exit of the inlet ($x = 0.308$ m) over the computation time of 6 ms. Two bulges are found in the outlet pressure distribution in Fig. 15b, corresponding to the arrival of the surging flow at the exit ($t = 0.5$ ms) and the formation of a near-axis normal shock wave ($t = 4$ ms). The abrupt increase in the inflow pressure seen at $t = 4$ ms in Fig. 15a indicates the rapid propagation of the influence of the incipient shock wave, which eventually leads to a fully choked

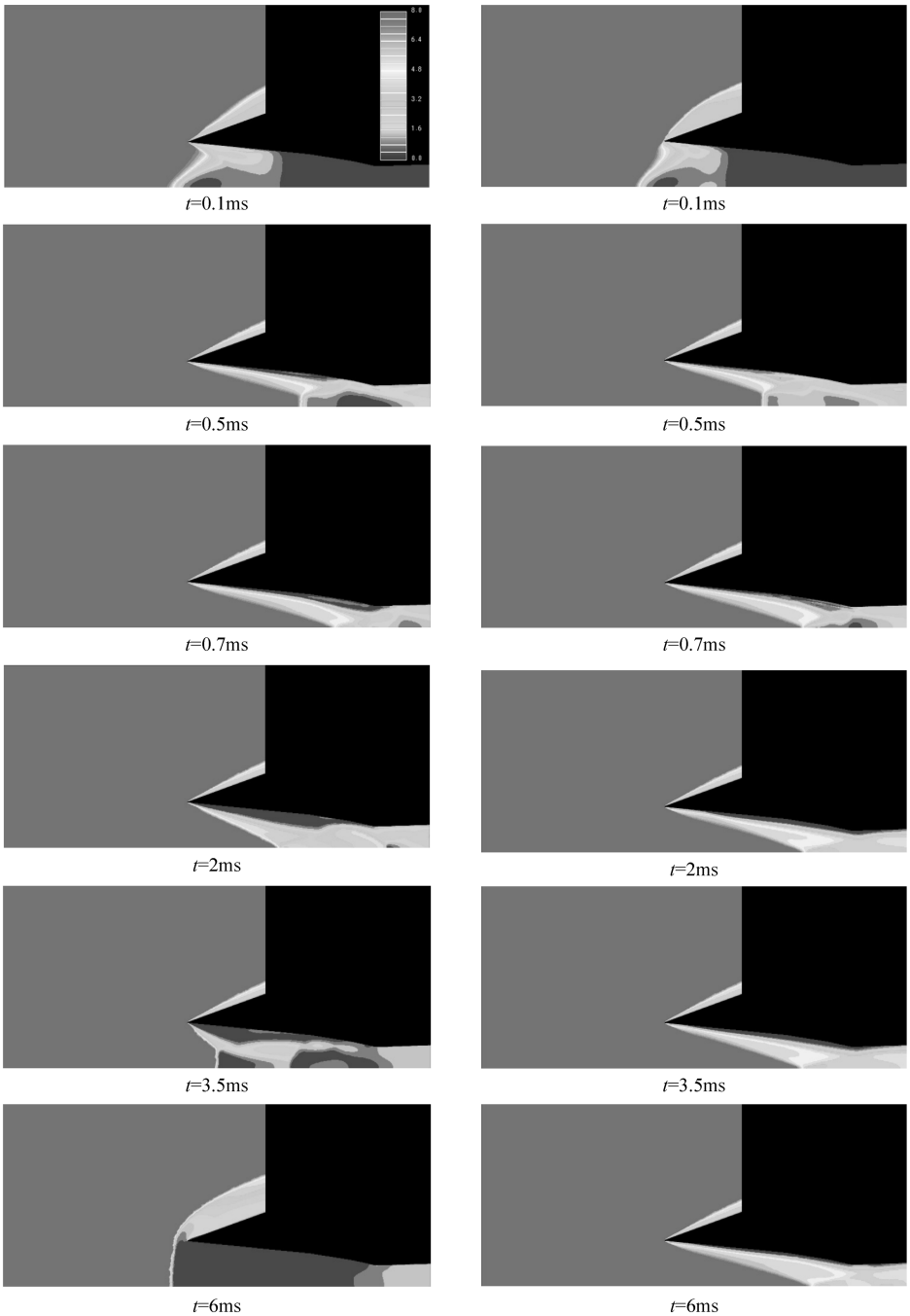

a) $p_i = 0.65p_\infty$ **b)** $p_i = 0.6p_\infty$

Fig. 12 Transient flowfields after conical diaphragm rupture ($\theta = 35°$).

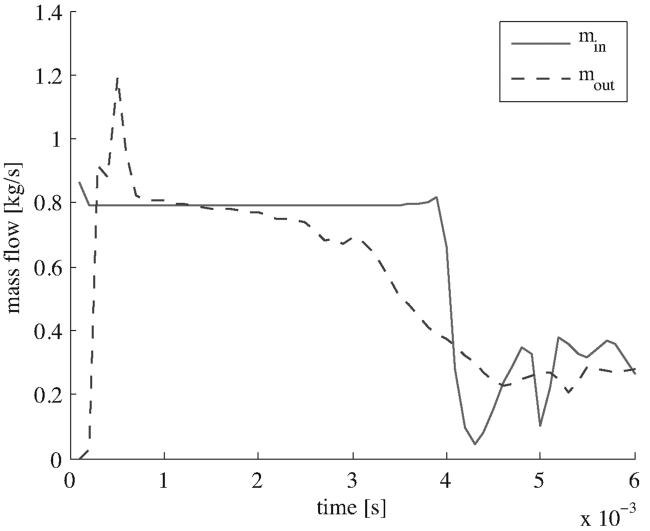

a) p_i=0.65p_∞

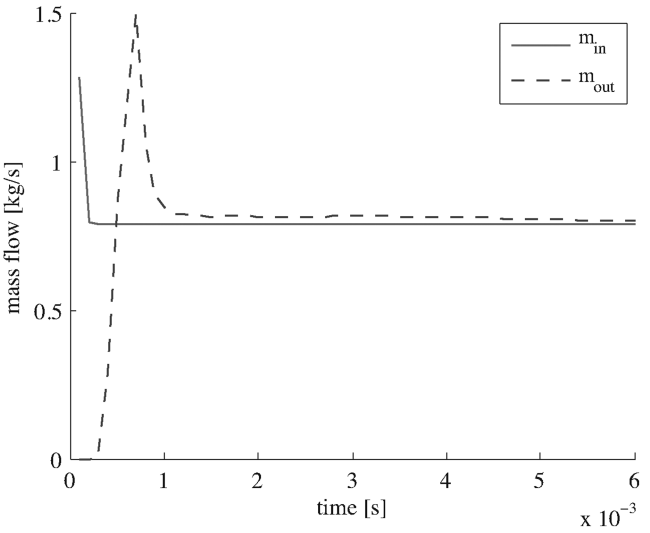

b) p_i=0.6p_∞

Fig. 13 Mass flow rates of inflow ($x = 0$ m) and outflow ($x = 0.308$ m) after diaphragm rupture ($\theta = 35°$).

flow. A trough can be seen at an offaxis location ($r \approx 0.05$ m) in the inflow pressure (Fig. 15a) during the relaxation and settlement period of the choked flow regime ($t = 5$–6 ms).

The internal pressure has then been reduced to 40% of the freestream. Representative transitional flowfields are shown in Fig. 16. After the initial rupture and flushing period ($t = 0.1$–0.5 ms), the boundary layer separates at the first compression corner, with the boundary layer quickly moving upstream, as does the oblique shock. However, at approximately $t = 1.5$ ms (Fig. 16a), this forward motion is suppressed with the shock reversing back downstream, with no normal shock being formed near the symmetry axis. The flow then enters a stabilization period ($t = 2$–6 ms), resulting in a successfully started state, as shown in Fig. 16b. The time progressions of the static pressure distributions at the inlet entrance and exit planes are shown in Fig. 17. It can be noted that the pressure at both stations settles at relatively low levels at an early stage, due to the absence of a bow shock wave, representing a distinct contrast with the unstarted case shown in Fig. 15.

c. $\theta = 70°$. Based on the observed trend between conical angle and internal starting pressure, 30% of the freestream has been chosen as the first internal pressure to be tested for a conical diaphragm angle of 70°. Unlike the previous two cases with smaller diaphragm angles, the shock wave is initially detached before rupture

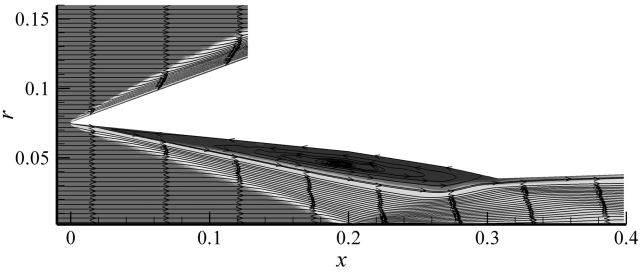

a) Recirculation at compression corners (t=2ms)

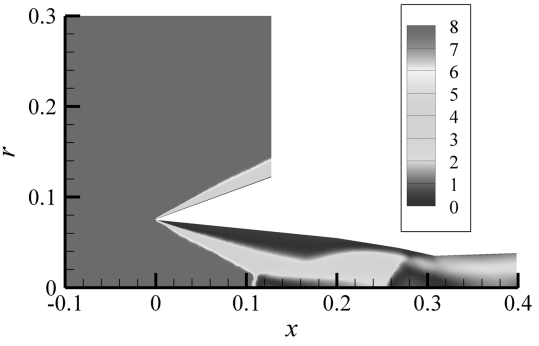

b) Onset of a normal shock wave (t=3.5ms)

Fig. 14 Transient flowfields after diaphragm rupture (Mach number distributions and streamlines, $\theta = 50°$, and $p_i = 0.5p_\infty$).

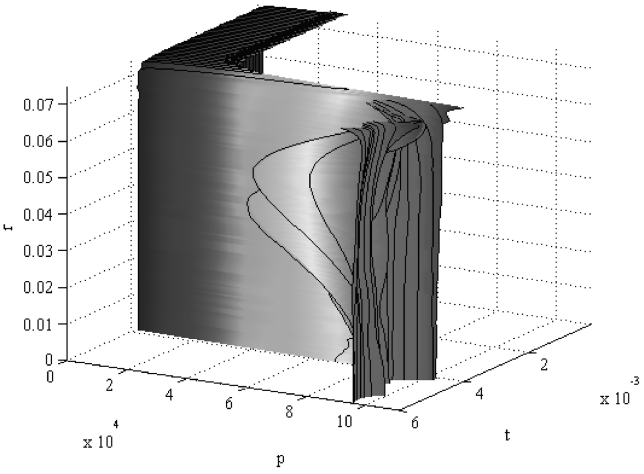

a) Inflow (x=0m)

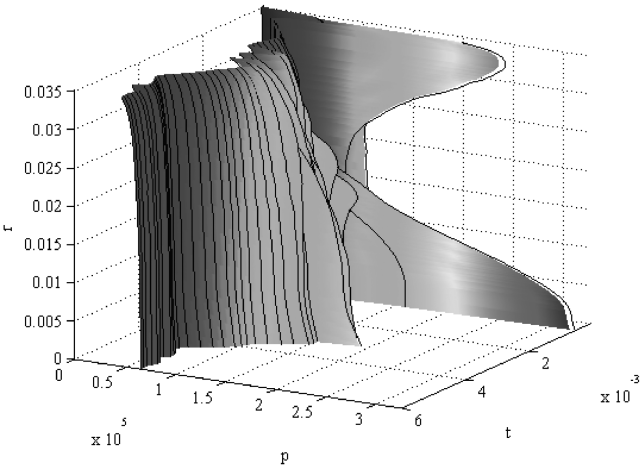

b) Outflow (x=0.308m)

Fig. 15 Static pressure distributions of transient flowfields after diaphragm rupture ($\theta = 50°$, and $p_i = 0.5p_\infty$).

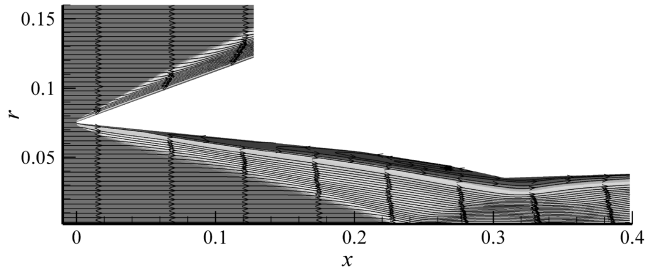

a) Streamlines for maximum separation (t=1.5ms)

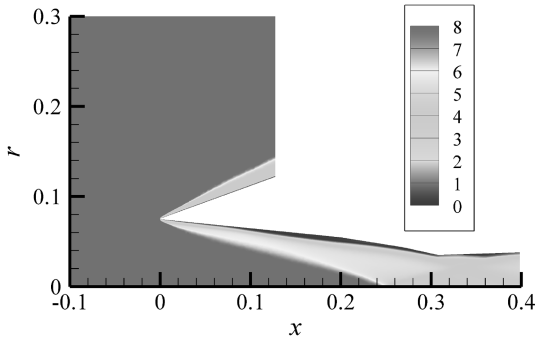

b) Started flow solution (t=6ms)

Fig. 16 Transient flowfields after diaphragm rupture (Mach number distributions and streamlines, $\theta = 50°$, and $p_i = 0.4p_\infty$).

in this case, as shown in Fig. 11. Subsequently, the boundary-layer separation is far more pronounced, reaching its zenith at approximately $t = 2$ ms after rupture, ensuring a higher-than-designed effective contraction ratio. The oblique shock continues to move upstream, with a normal shock wave starting to form at the axis of symmetry at approximately 3 ms. The normal shock continues to move upstream ($t = 3$–5 ms), increasing the effective strength of the oblique shock, until both shocks join into one entity. A stabilization period follows from $t = 5$–6 ms, resulting in an unstarted solution, with a strong bow shock forming with subsonic flow entering the throat.

The internal pressure has then been reduced to 25% of the freestream, with the resulting flowfield being nearly identical to that outlined for the 50° diaphragm at the internal pressure of 40% of freestream (Fig. 16), with the forward motion of the oblique shock being suppressed, with no normal shock being formed near the symmetry axis. The magnitude of separation is also much smaller than the case of the internal pressure of 30% of freestream, resulting in a much milder effective contraction ratio.

d. $\theta = 90°$. A diaphragm with an angle of 90°, i.e., normal diaphragm, is tested as the last instance for a diaphragm angle variation study. The before-rupture shock wave is detached, with subsonic conditions present downstream of the shock in this case, too, as expected by the conical shock relations. Initially, the internal pressure p_i has been dropped to 10% of the freestream. For this case, a started flow regime has been achieved after 6 ms, similar to what have been observed for the 50 and 70° cases. The initial internal pressure has then been ramped up to 25%, where an unstarted flow regime may well be anticipated, according to the trend observed at lower diaphragm angles. The flowfield, on the contrary, has resulted in a started flow in this case as well. An unstarted flow has eventually been observed after rupture when the initial internal pressure has been raised to 30%. The maximum allowable pressure, above which the inlet ceases to start with diaphragm rupture, thus has been located to lie between 25 and 30% in this case.

The state of the inlet as a result of diaphragm rupture is summarized in Fig. 18 for the cases investigated in this parametric study, with respect to the diaphragm angle θ and the pressure ratio between the internal pressure and the freestream (p_i/p_∞). A distinct correlation between the two parameters can be seen; the maximum allowable internal pressure diminishes as the diaphragm angle

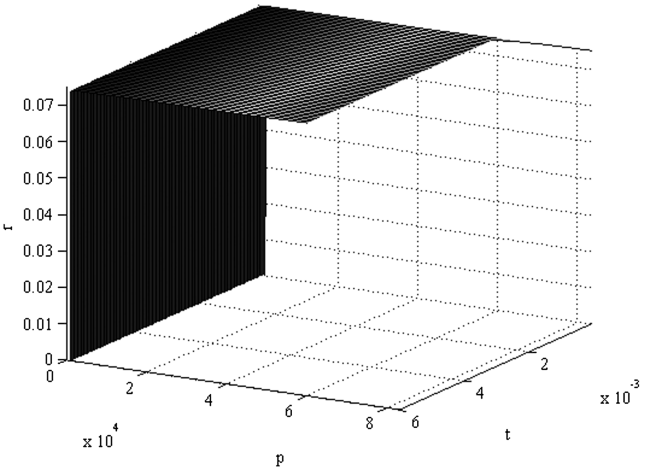

a) Inflow (x=0m)

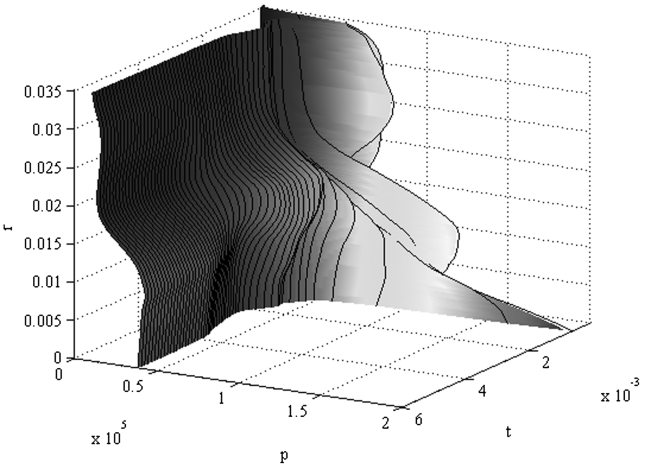

b) Outflow (x=0.308m)

Fig. 17 Static pressure distributions of transient flowfields after diaphragm rupture ($\theta = 50°$, $p_i = 0.4p_\infty$).

increases, in accordance with the trend reported for an inviscid study previously undertaken by Tahir et al. [15]. However, the maximum allowable pressure becomes independent of the diaphragm angle at higher angles, where shock waves are detached from the diaphragms in the steady flowfields before rupture.

The static and total pressure ratios across the shock wave as well as the shock wave angle θ_s are plotted for the inflow of $M_\infty = 8$ in Fig. 19 with respect to the conical diaphragm angle θ from the conical shock relations, where the subscript c denotes the properties at the

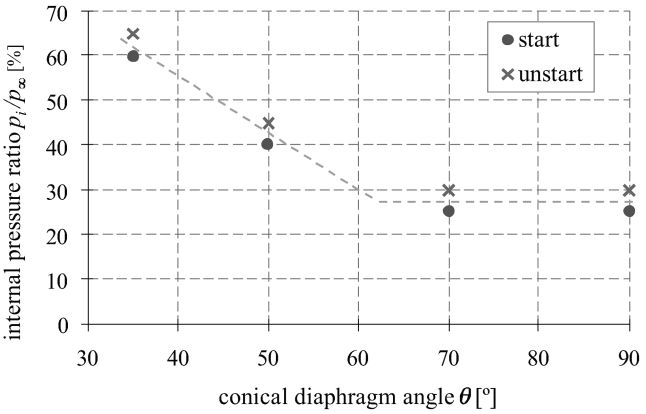

Fig. 18 Inlet startability of the diaphragm rupture method with respect to conical diaphragm angle θ and internal pressure ratio p_i/p_∞.

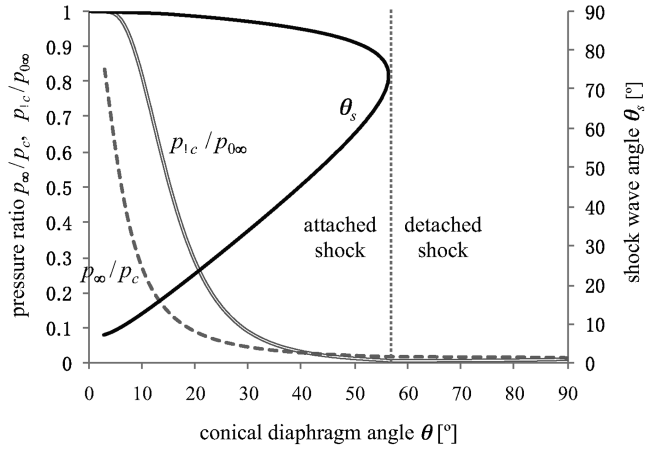

Fig. 19 Variations of shock wave angle θ_s, static pressure ratio p_∞/p_c and total pressure ratio $p_{0c}/p_{0\infty}$ at $M_\infty = 8$ from conical shock relations.

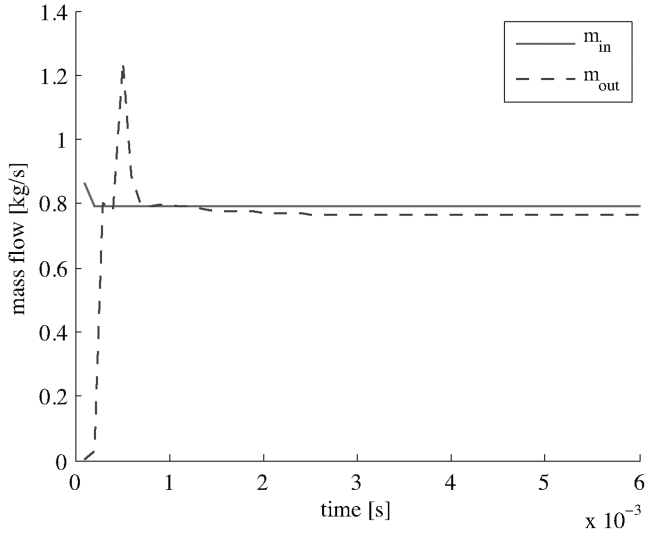

Fig. 20 Mass flow rates of inflow ($x = 0$ m) and outflow ($x = 0.308$ m) after diaphragm rupture with bleed ($\theta = 35°$ and $p_i = p_\infty$).

surface immediately upstream of the diaphragm (note that the static pressure ratio is inverse for plotting purposes). It can be seen that the static pressure increases (hence pressure difference across the diaphragm increases) and total pressure decreases across the shock wave monotonically up to $\theta = 56°$, above which angle the before-rupture shock wave detaches from the diaphragm surface and both the static and total pressure ratios level off. This tendency suggests some correlation between the maximum allowable internal pressure and the static or total pressure, but further investigation is needed to identify the driving factor.

2. Bleed-Slot Addition

a. Effects of Bleed. The addition of bleed to viscous flow has been found to be able to effectively induce a started solution for conditions in which unstart would normally occur, for a given conical diaphragm angle [18]. In this case, successful starting was achieved at 65% of the freestream pressure, for a conical diaphragm angle of 35°, whereas the maximum allowable pressure was 60% for viscous flow. The aim now is to find the maximum permissible pressure, with the addition of an annular bleed, which is installed at the conjunction between the first and second ramps, spanning over 37% of the second ramp in length (40% in terms of area), as shown in Fig. 4.

By iteratively increasing the internal pressure, it has been found that the bleed slot can induce a started solution at 100% of the freestream pressure. The flowfield solution over time has been observed to be invariably similar to that of the 65% case. The addition of bleed drains off the low-momentum regions that have been seen to accumulate at the compression corners for the nonbleed cases, as early as 0.7 ms after rupture. A supersonic flow regime is then achieved, with the solution remaining stable from then on (t= 2–6 ms). In this case, no upstream motion of the oblique shock structure after diaphragm rupture is observed, with negligible boundary-layer separation occurring. Following this encouraging result, the amount of mass flow deficit is of primary interest, as this is directly linked with the loss of thrust production. The variations of the mass flow rates are plotted in Fig. 20, which shows a difference between the inflow and outflow rates of approximately 0.025 kg/s, indicating that effectively 3.13% of the incoming mass flow has been discharged through the bleed slot. This is a relatively small amount in consideration of the large gain obtained in the maximum allowable pressure.

Table 1 Mass flow rates of inflow and outflow with various bleed-slot lengths

Bleed-slot length (% of original)	Inflow mass flow rate, kg/s	Outflow mass flow rate, kg/s
100	0.79017	0.7655
75	0.79017	0.7716
50	0.79017	0.7765
25	0.79017	0.7800

b. Bleed-Slot Length Study. For the purposes of this study, an internal pressure of 90% of the freestream is used with a reduction safety factor of 10% applied to the condition used in Sec. III.A.2.a, where the inlet has been observed to start at an internal pressure of 100% of the freestream value for a conical angle θ of 35°. A started flow regime has been achieved with a bleed slot of 75, 50, and 25% of the initial slot length, while inlet unstart has occurred with a bleed slot of a size 12.5% of the initial length.

The mass flow at the entrance ($x = 0$ m) and exit ($x = 0.308$ m) of the inlet has been calculated for each bleed-slot length computation and tabulated in Table 1. The mass flow deficit due to the addition of bleed has been plotted with respect to the length of the bleed slot in Fig. 21. The mass flow deficit can be seen to decrease in a linear manner as the slot size diminished, reaching 1.29% at the slot length of 25% of the original, which represents a negligible penalty in regard of the thrust. It can be noted that this linear decrease suggests choked flow conditions at the slot and hence a constant mass flow discharge rate per length.

B. Variable Geometries

1. Opening Doors

The progression of the transitional flowfields during the door opening process is displayed by Mach number distributions in

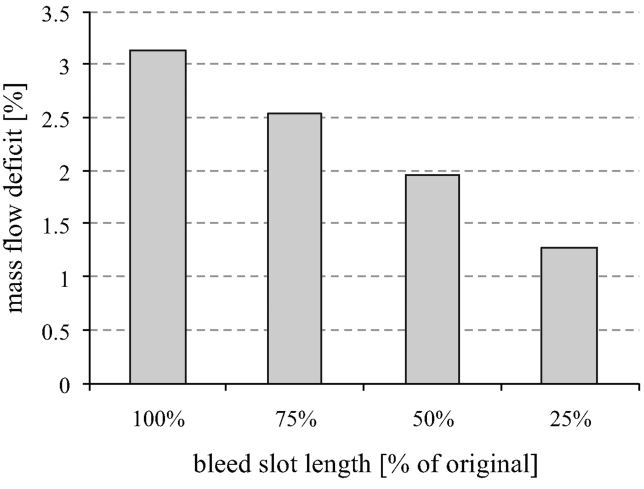

Fig. 21 Mass flow deficit with various bleed-slot lengths.

t=0ms

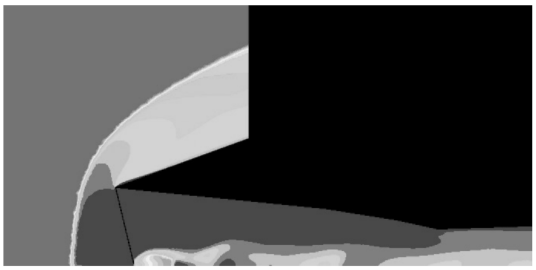

t=20ms

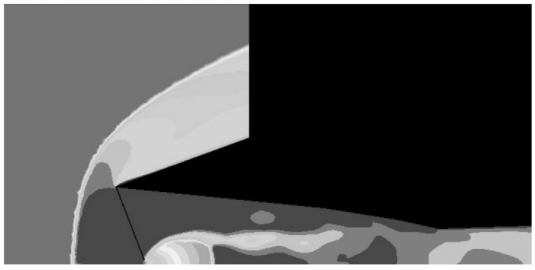

t=25ms

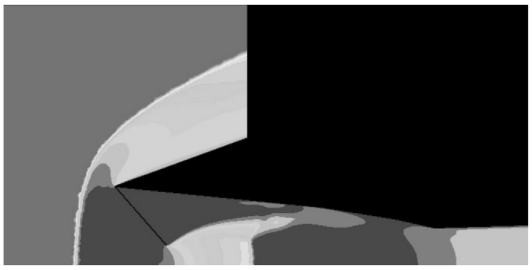

t=35ms

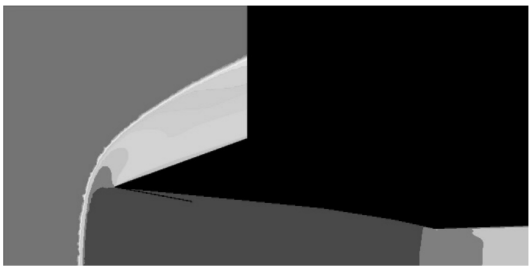

t=50ms

Fig. 22 Transient flowfields during door opening (Mach number distributions).

Fig. 22. The steady flowfield before opening ($t = 0$ ms) is essentially the same as that with a normal diaphragm case, characterized by a strong bow shock formed in front of the inlet. As the door opens, the high-pressure gas between the shock and door surges into the inlet. The flow acceleration through the opening leads to the formation of a barrel shock wave, which grows continuously to some extent, its size peaking at approximately $t = 25$ ms. After this, the barrel shock wave decays as the aperture increases and thus flow acceleration decreases, with the front of the barrel shock moving relatively slowly downstream ($t = 35$ ms). The barrel shock structure eventually fades

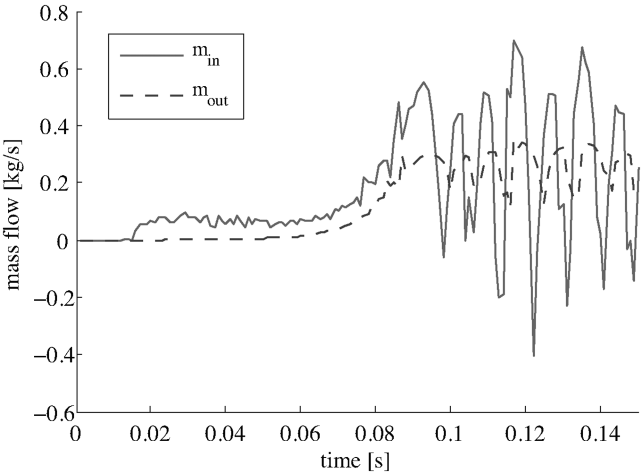

Fig. 23 Mass flow rates at the inlet entrance ($x = 0$ m) and exit ($x = 0.308$ m) during and after door opening.

out when the aperture ceases to provide adequate acceleration and the nearly stagnant flow behind the primary bow shock becomes dominant inside the inlet, resulting in a fully choked inlet ($t = 50$ ms).

Plotted in Fig. 23 is the history of the mass flow rates monitored at the entrance ($x = 0$ m) and exit ($x = 0.308$ m) during the transition. It can be seen that the inflow mass rate stays relatively constant during the development and decay of the barrel shock structure ($t = 20$–40 ms), followed by a large oscillation even after the flow inside the inlet becomes fully subsonic, hence choked ($t \geq 50$ ms), when the bow shock wave keeps bouncing back and forth upstream of the inlet, inducing flow unsteadiness. The flowfield finally settles down after a long relaxation period, the mass flow rates ending up at considerably low levels (about 0.2 kg/s), comparable to those previously observed in the unstarted case (e.g., Fig. 13a).

2. *Sliding Doors (Diaphragm Erosion)*

The third variable-geometry approach investigated in the present study is to open the inlet aperture by means of sliding doors.[††] The progression of transitional flowfields induced by this method is displayed in Fig. 24. Initially, the inlet is completely sealed with a door fully closed at $t = 0$ ms. The external air flows into the channel as the door is retracted upward ($t \geq 10$ ms). It can be seen that the channel is constantly filled with hypersonic airflow with the same Mach number as the freestream value, that is, $M_\infty = 8$, with no presence of a shock wave observed throughout the passage. The region behind the door is dominated by stagnant fluids, which constantly diminish with the opening of the aperture and eventually disappears when the door is fully retracted ($t = 50$ ms).

The mass flow rates monitored at the entrance and exit of the inlet are plotted in Fig. 25. It can be seen that the inflow and outflow rates constantly increase at the same rate, closely linked with each other with negligible difference throughout the process. This feature represents a high degree of quasi-steadiness of the flowfield. The flow rates level off at high values close to 0.8 kg/s after the completion of the door motion ($t > 50$ ms), comparable to that shown in Fig. 13b, indicating a successfully started inlet.

The high efficacy of this method in starting the inlet can be traced to the effective contraction ratio between the inflow and outflow, which is regulated by the variable aperture. Figure 26 shows the path of the area contraction during the process, superimposed in the Kantrowitz diagram. The area ratio between the outflow and inflow (A^*/A_i) is, in effect, higher than 1 at the early stage of the process,

[††]This method is analogous to a conical diaphragm with a forward-pointed sharp tip that is gradually eroded from the vertex, due to the aerothermal heat experienced on the surface, where deformation occurs in finite length of time and the associated flowfield is inherently different from that in the case of instantaneous diaphragm rupture.

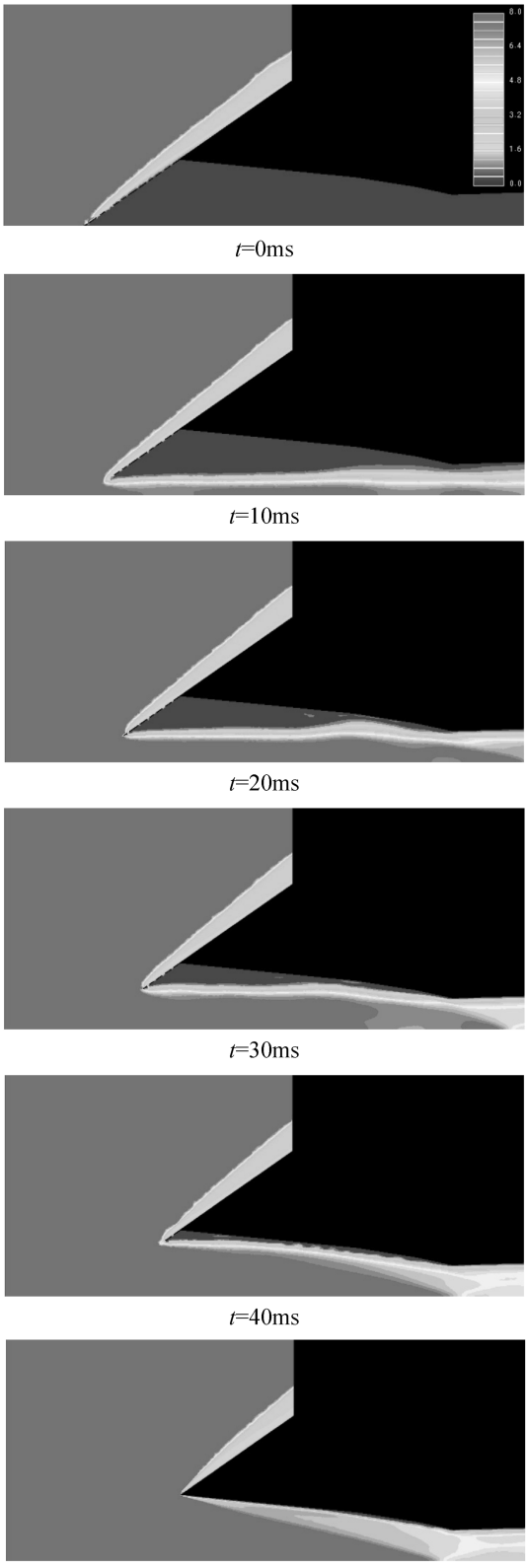

Fig. 24 Transient flowfields during sliding-door opening (Mach number distributions).

due to the small inflow aperture A_i, which allows to position the inlet well above the Kantrowitz limit, where the inlet starts spontaneously. As the sliding door opens, the increasing aperture brings the contraction ratio down across the Kantrowitz line into the dual solution zone, where both started and unstarted states can be possible. The inlet, which has already been started, remains operational even in this zone, leading to successful starting.

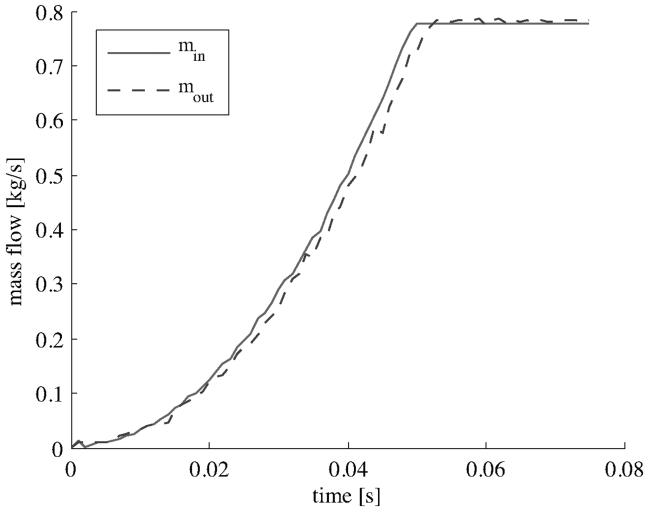

Fig. 25 Mass flow rates at the inlet entrance ($x = 0$) and exit ($x = 0.308$) during sliding-door opening.

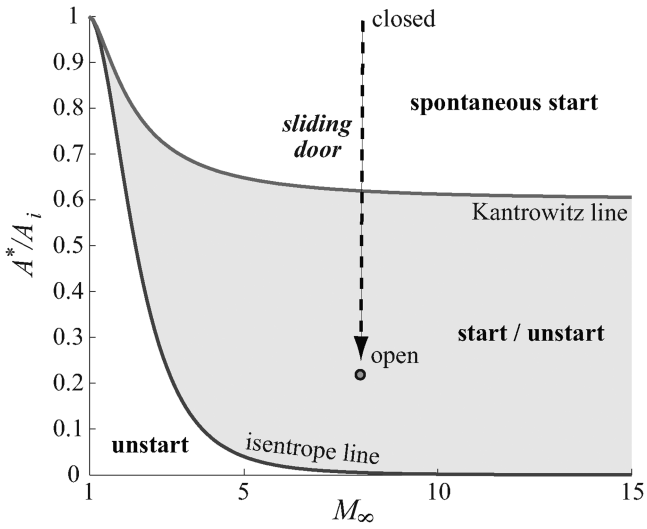

Fig. 26 Sliding-door process in Kantrowitz diagram.

IV. Conclusions

A variety of starting methods based on two principles, i.e., unsteady effects and variable geometries, have been examined for axisymmetric scramjet inlets in a hypersonic flight condition at Mach 8. Time-accurate computations including viscous effects have been performed to probe the transitional flowfields and investigate the capability of these techniques to start the scramjet inlet.

Instantaneous rupture of conical (and normal) diaphragms has been tested as a method to induce highly unsteady flow phenomena with a high spatial pressure gradient. Started inlet flows have been achieved under certain conditions, circumventing the Kantrowitz criterion, which theoretically prescribes the inlet flow state in quasi-steady assumptions. A parametric study has been conducted with respect to the semivertex diaphragm angle and the internal stagnation pressure of the air sealed by the diaphragm. The maximum allowable internal pressure, under which starting occurs, has been found to decrease monotonically as the diaphragm angle increases up to the maximum angle for attached shock waves. This tendency may be related to the static or total pressure ratio across the diaphragm, but the key factor is yet to be identified by further investigation. The effect of a bleed-slot addition to the compression corner has been investigated, in combination with the diaphragm rupture method. A parametric study with various slot lengths has demonstrated high effectiveness of boundary-layer bleeding combined with diaphragm rupture, where a bleed through a small slot is found to be capable of

starting the inlet with a higher internal pressure at the cost of negligible loss of mass flow and hence thrust.

Several methods using variable inlet geometries have been investigated as alternative means to start the inlet. Opening a door that rotates around the hinge anchored at the leading edge of the inlet has been tested, but it has resulted in a fully choked, hence unstarted, inlet that is unable to induce drastic impact on the flowfield that has been predominated by a strong bow shock. The second method that has been tested is sliding a door with a conical contour that opens up a circular aperture from the symmetry axis. Note that these two methods are similar, except that the former aims to accelerate subsonic flow into the stagnant flow in the inlet and not succeeding, whereas the latter case features supersonic flow that can push through with its high momentum without the need for acceleration. A quasi-steady flowfield has been observed throughout the process, with hypersonic airstream maintained throughout the flow passage, due to milder effective flow contraction moderated by the variable geometry. Consequently, a started inlet state with a supersonic flow regime has successfully been established in a highly reliable manner by using this method.

References

[1] Paull, A., Alesi, H., and Anderson, S., "HyShot Flight Program and How It Was Developed," AIAA Paper 2002-5248, Sept. 2002.

[2] Boyce, R. R., Gerard, S., and Paull, A., "The HyShot Scramjet Flight Experiment—Flight Data and CFD Calculations Compared," AIAA Paper 2003-7029, Dec 2003.

[3] McClinton, C. R., "X-43—Scramjet Power Breaks the Hypersonic Barrier: Dryden Lectureship in Research for 2006," AIAA Paper 2006-1-317, Jan. 2006.

[4] Hunt, D. C., Paull, A., Boyce, R. R., and Hagenmaier, M., "Investigation of an Axisymmetric Scramjet Configuration Utilising Inlet-Injection and Radical Farming," *Proceedings of the 19th International Symposium on Airbreathing Engines*, Montréal, Sept. 2009, pp. 1353-1–1353-10.

[5] Odam, J., and Paull, A., "Radical Farming in Scramjets," *Notes on Numerical Fluid Mechanics and Multidisciplinary Design*, edited by C. Tropea, S. Jakirlic, H-J Heinemann, and H. Hinlinger, Vol. 96, Springer, Berlin, 2007, pp. 276–283.

[6] McGuire, J. R., Boyce, R. R., and Mudford, N. R., "Radical Farm Ignition Processes in Two-Dimensional Supersonic Combustion," *Journal of Propulsion and Power*, Vol. 24, No. 6, 2008, pp. 1248–1257. doi:10.2514/1.35562

[7] Tahir, R. B., *Starting and Unstarting of Hypersonic Air Inlets: An Illustrated Guide to Flow Starting Phenomena in the Axisymmetric Busemann Geometry and Other Perforated Diffusers*, VDM Verlag, Saabrücken, Germany, 2009.

[8] Kantrowitz, A., and Donaldson, C., "Preliminary Investigation of Supersonic Diffusers," NACA ACR-L5D20, May 1945.

[9] Kantrowitz, A., "The Formation and Stability of Normal Shock Waves in Channel Flows," NACA TN 1225, March 1947.

[10] Veillard, X., Tahir, R. B., Timofeev, E. V., and Mölder, S., "Limiting Contractions for Starting Simple Ramp-Type Scramjet Intakes with Overboard Spillage," *Journal of Propulsion and Power*, Vol. 24, No. 5, 2008, pp. 1042–1049. doi:10.2514/1.34547

[11] Mölder, S., Timofeev, E. V., and Tahir, R. B., "Flow Starting in High Compression Hypersonic Air Inlets by Mass Spillage," AIAA Paper 2004-4130, July 2004.

[12] Najafiyazdi, A., Tahir, R., Timofeev, E. V., and Mölder, S., "Analytical and Numerical Study of Flow Starting in Supersonic Inlets by Mass Spillage," AIAA Paper 2007-5072, July 2007.

[13] Van Wie, D. M., and Mölder, S., "Applications of Busemann Inlet Designs for Flight at Hypersonic Speeds," AIAA Paper 92-1210, Feb. 1992.

[14] Van Wie, D. M., "Scramjet Inlets," *Scramjet Propulsion*, edited by E. T. Curran, and S. N. B. Murthy, Vol. 189, Progress in Astronautics and Aeronautics, AIAA, Reston, VA, 2000, pp. 447–511.

[15] Tahir, R. B., Mölder, S., and Timofeev, E. V., "Unsteady Starting of High Mach Number Air Inlets—A CFD Study," AIAA Paper 2003-5191, July 2003.

[16] Timofeev, E. V., Tahir, R. B., and Mölder, S., "On Recent Developments Related to Flow Starting in Hypersonic Air Intakes," AIAA Paper 2008-2512, Apr 2008.

[17] Baig, S., and Timofeev, E. V., "A Simple Moving Boundary Technique and Its Application to Supersonic Inlet Starting," *Proceedings of the 16th Annual Conference of the CFD Society of Canada*, Saskatchewan, Canada, June 2008.

[18] Ogawa, H., Grainger, A. L., and Boyce, R. R., "Numerical Investigation of Viscous Effects on Scramjet Inlet Starting," *Proceedings of the 2009 Asia-Pacific International Symposium on Aerospace Technology*, Gifu, Japan, Nov. 2009, pp. 550–557.

[19] CFD++, Software Package, Ver. 8.11, Metacomp Technologies, Inc., Agoura Hills, CA, 2009.

[20] Boyce, R. R., and Hillier, R., "Shock-Induced Three-Dimensional Separation of an Axisymmetric Hypersonic Turbulent Boundary Layer," AIAA Paper 2000-2226, June 2000.

[21] Pointwise, Software Package, Ver. 16.02, Pointwise, Inc., Fort Worth, TX, 2008.

R. Bowersox
Associate Editor